

## **CHAPTER 5**

### **MECHANICS OF INDENTATION**

Michelle L. Oyen

*Department of Engineering, Cambridge University  
Trumpington Street, Cambridge, UK  
E-mail: mlo29@cam.ac.uk*

The fundamental contact mechanics underlying nanoindentation testing techniques are reviewed. A range of material constitutive responses are covered, including elastic, plastic, and viscous deformation, and incorporating indentation of linearly viscoelastic materials and poroelastic materials. Emphasis is on routine analysis of experimental nanoindentation data, including deconvolution techniques for material properties measurements during indentation. In most cases, an analytical approach for an isotropic half-space is considered. Special cases are briefly described, including anisotropic materials, inhomogeneous composite materials and layered film-substrate systems.

#### **1. Introduction**

Experimental contact mechanics measurement of material properties has become extremely popular in the last decade, due to both the commercialization of dedicated instrumented indentation testing devices and advances in the practical and experimental understanding of performing contact mechanics experiments. Many commercial indenters are set-up as “black-box” instruments for routine mechanical testing, in which data analysis is automated and “the mechanical properties” are directly exported from the instrument. However, it is extremely important to review the underlying contact mechanics that are used in indentation data analysis for several reasons. First, although an elastic-

plastic analysis (typically based on the method of Oliver and Pharr<sup>1</sup>) can be used to obtain numerical values for the elastic modulus ( $E$ ) and hardness ( $H$ ) of just about any sample placed into the indenter, an elastic-plastic analysis may be inappropriate for the material (given its constitutive behavior, which may or may not be elastic-plastic) and the numbers thus obtained are “garbage in, garbage out.” As most biological materials are not well-described by an elastic-plastic response—with perhaps the exceptions of dried plant materials and biomineral composites with large mineral fractions—other analyses are often more appropriate than an elastic-plastic analysis<sup>2</sup>.

This chapter will provide a background in contact mechanics—including elastic, plastic and time-dependent deformation—with an emphasis on experimental applications of contact mechanics. As such, there will be no effort to derive key equations, and the reader is referred to other works on contact mechanics<sup>3,4</sup> for derivations and methods of deriving the equations presented. The chapter starts with the practical, experimental considerations of tip geometry and loading function selection, and how these selections influence indentation data analysis. Next, elastic contact mechanics is considered, including solutions for indenting elastic half-spaces with tips of different geometries as well as for more complicated, inhomogeneous geometries. Next, more complicated constitutive responses are considered, including elastic-plastic, linear and nonlinear viscoelastic, and poroelastic contact mechanics. The chapter concludes with considerations of time-dependent contact deformation, including viscoelastic and poroelastic approaches that have been used for the study of hydrated biological tissues<sup>5,6</sup>.

## **2. Practical considerations**

In this section, two practical considerations are explored: probe tip geometry and time-history of the loading function during contact. Indentation data analysis is based in part on the geometry of the contact, and as such the choice of indenter tip geometry is a crucial consideration in designing any indentation experiment. For an elastic solid, the time-history of the loading function is irrelevant and the choice can be made

based on convenience; however, for time-dependent materials the loading history is integrated into the data analysis and must be considered in further detail.

### 2.1. Indenter probe geometry

Indentation testing considers the contact between a probe and the sample. The probe geometry thus determines the deformation profiles obtained during the test, and as such is an extremely important experimental controllable. Flat punch tips are convenient in that the cross-sectional area of the contacted region is constant, simplifying analysis. However, due to the sharp corners, there can be stress singularities at the edges. Particularly in extremely small-scale nanoindentation testing, it can also be nearly impossible to align the tip's flat surface parallel to the sample surface. Therefore two tip shapes dominate small-scale contact testing: spherical and conical or pyramidal (Figure 5-1).

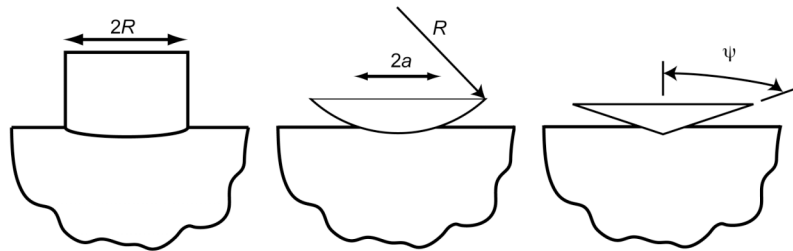


Figure 5-1. Schematic illustrations of cylindrical, spherical and conical or pyramidal indenter geometries. The critical parameters are the indenter radius,  $R$ , for a cylindrical or spherical indenter, the contact radius  $a < R$  for a spherical indenter, and the included indenter half-angle  $\psi$  for a conical indenter (or effective indenter half-angle for a pyramidal indenter).

Spherical tips are advantageous in that there is a delayed onset of plastic deformation, while conical or pyramidal tips are exactly the opposite since there is usually an immediate onset of plasticity and thus elastic-plastic deformation even at small displacements. In indentation testing with conical or pyramidal tips there is also the advantage of geometric similarity—there is no intrinsic length-scale associated with the size of the tip, and indentation tests at large loads result in

deformation patterns that are scaled up from indentation tests at small loads. A disadvantage in the use of spherical and conical tips is that load is no longer a linear function of displacement, as is the case for a homogeneous tensile test or a flat-punch indentation test, due to the changes in tip-sample contact area as the tip is pressed further into the surface. These load-displacement functional forms for different indenter tip geometries—and thus the data analysis options for each tip—will be explored further in section 3 of this chapter.

## 2.2. Load functions

The second critical experimental controllable in indentation testing, as in any sort of mechanical testing, is the input loading function. Commercial nanoindentation instruments are essentially load-controlled, in stark contrast to the displacement-control used in servohydraulic universal test-frames. Because the probe is pressed into the sample and then retracted, the indentation cycle is most commonly considered as a load-unload cycle. Standard tests are for ramping at constant loading and unloading rates, ramping to a peak load and then holding for a fixed time before unloading, and loading exponentially:

$$P(t) = P_0 \exp(rt) \quad (5-1)$$

where  $P_0$  is an extremely small tare load at the which the test commences and  $r$  is the effective strain rate. This loading condition (Eqn. 5-1, Fig. 5-2c) approximates a constant indentation strain-rate under geometrically similar indentation with constant material hardness<sup>7</sup>. Some nanoindentation systems are equipped with a feedback-control mechanism, which allows for displacement-controlled indentation testing. Again the displacement can be ramped up and down at fixed rate, and can potentially include a holding period at peak displacement, resembling Figure 5-2 (a and b) but with displacement replacing load as the controlling variable along the y-axis.

In addition to the quasistatic indentation conditions presented in Figure 5-2, a number of indentation loading schemes include dynamic loading, typically as a sinusoidal variation in the load. The sinusoidal loading can be of quite small amplitude, and is then superposed on top of

an existing quasistatic load function to increase the amount of information obtained from a single indentation test. For example, small-amplitude sinusoidal loading superimposed on the holding segment of a trapezoidal load function (Fig. 5-2b) can be used to measure the dynamic response of a viscoelastic material, giving the real and imaginary parts of the complex modulus ( $E^*(\omega)$  where  $\omega$  is the sinusoidal loading frequency; see section 6.1.3 below). This mode of dynamic testing will be discussed later in this chapter. First, we examine the elastic contact mechanics expressions as a function of indenter tip shape.

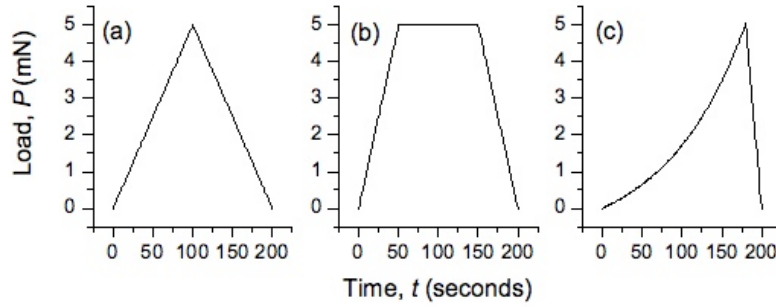


Figure 5-2. Load-time profiles for (a) a simple load-unload cycle under triangular loading, (b) a trapezoidal load-hold-unload profile in which creep can be measured during the holding period, and (c) exponential loading.

### 3. Elastic Contact

Much of the work on elastic contact originated with the work of Hertz in the late 19<sup>th</sup> century<sup>8</sup>. An excellent overview is presented in the text of Johnson<sup>4</sup>. The work of Hertz concerned the contact of two bodies with effectively spherical profiles, in which an effective radius  $R$  is defined in the context of the radii of the two bodies ( $R_1, R_2$ ) as:

$$\frac{1}{R} = \frac{1}{R_1} + \frac{1}{R_2} \quad (5-2)$$

Similarly, the elastic modulus of the contact is defined by the series combination of the plane strain moduli of the two bodies:

$$\frac{1}{E_R} = \frac{1 - \nu_1^2}{E_1} + \frac{1 - \nu_2^2}{E_2} \quad (5-3)$$

where  $\nu_i$  is the Poisson's ratio and  $E_i$  is the elastic modulus for each body, and for which isotropic elasticity has been assumed. (Note the direct analogy to equation 2-9 in chapter 2 of this volume.) In the following sections we will see how these ideas have influenced modern nanoindentation testing. To continue with the Hertzian contact theme, we will start with spherical indentation before moving on to consider flat punch and conical/pyramidal indentation. As noted in the introduction to this chapter, the mechanisms for solving elastic contact problems will not be considered here, only the solutions at textbook-level. In addition to the texts mentioned earlier<sup>3,4</sup>, the reader is also referred to the classic work of Sneddon<sup>9</sup> concerning elastic contact.

### 3.1. Spherical (Hertzian) Elastic Contact

In the limit of a spherical indenter on a half-space, Eqn. 5-2 reduces to  $R = R_i$  where  $R_i$  is the indenter tip radius. The indenter is typically penetrated only a small fraction of its radius into the material, such that the projected contact radius ( $a$ ) is much smaller than the indenter radius. The contact radius can be related to the radius ( $R$ ) and total indentation depth ( $h$ ) as:

$$a = \sqrt{Rh} \quad (5-4)$$

The load-displacement ( $P$ - $h$ ) relationship for spherical (Hertzian contact) indentation is:

$$P = \frac{4\sqrt{R}}{3} \frac{E}{(1 - \nu^2)} h^{3/2} \quad (5-5)$$

In this case, the indenter has been assumed to be much stiffer than the sample ( $E_s \ll E_i$ ) such that the reduced modulus  $E_R$  is simply the plane strain modulus for the sample,  $E_R = E_s / (1 - \nu_s^2)$ .

For a perfectly elastic spherical indentation experiment, the load-displacement response can be fit to equation 5-5 directly (Figure 5-3). One mechanism to determine if the contact is perfectly elastic is to estimate the indentation strain  $\epsilon_i$  as:

$$\epsilon_i = 0.2(a / R) = 0.2(h / R)^{1/2} \quad (5-6)$$

At small strains, the yield stress has not been reached and the contact is perfectly elastic. When the yield stress has been reached, the functional form of the load-displacement response shifts due to dominant plastic deformation, as will be discussed further in section 4.1.

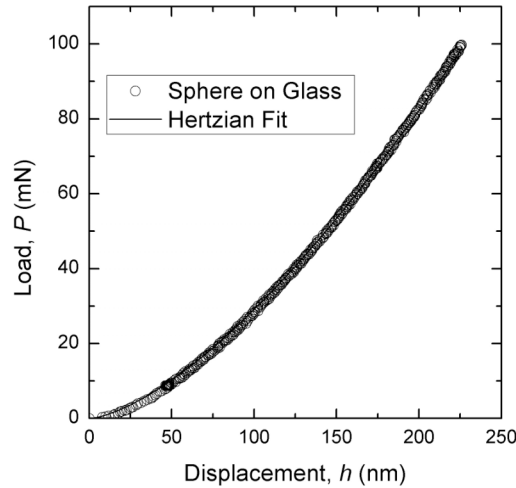


Figure 5-3. Perfectly elastic (Hertzian) contact on glass, in load-displacement ( $P$ - $h$ ) coordinates, showing the fit to Eqn. 5-5.

### 3.2. Flat Punch Elastic Contact

Although not often used on stiff materials at the nano-scale, flat punch indentation is occasionally utilized for extremely compliant materials, including hydrogels and hydrated biological tissues. The load-displacement response for a cylindrical indenter with radius  $R$  is:

$$P = 2R \frac{E}{(1-\nu^2)} h \quad (5-7)$$

In contrast to the Hertzian case, in which the relationship between load and displacement is not linear, the constant contact area means that in the flat punch case, the load-displacement response is linear.

### 3.3. Sharp Elastic Contact

Most commonly a sharp indenter tip—either a cone or a three-sided pyramid—is used in nanoindentation. The three-sided pyramid, called a “Berkovich” tip, was designed to mimic the relationship between indentation depth and projected contact area as is found for a Vickers pyramid—the four-sided pyramid most commonly used in classic microindentation hardness experiments. The full elastic solution for conical indentation is<sup>9</sup>:

$$P = \frac{\pi \tan \psi}{2\gamma^2} \frac{E}{(1-\nu^2)} h^2 \quad (5-8)$$

for a conical indenter with included half-angle  $\psi$  and where  $\gamma = \pi/2$ .

## 4. Elastic-Plastic Contact

The standard metric for evaluating the extent of plastic deformation in an indentation test is by the “hardness” which is representative of the resistance to plastic deformation, and can be related to a metal’s yield stress. In microindentation, the residual indentation impression is measured with an optical microscope, and the hardness—a representative contact stress—is computed as the ratio of indentation load to projected area<sup>10</sup>:

$$H = \frac{P_{\max}}{2b^2} = \frac{P_{\max}}{\pi a^2} \quad (5-9)$$

where  $b$  is half the length of the impression diagonal for a Vickers four-sided pyramid, or  $a$  is the effective contact radius for a circular impression. In soft metals, the bulk of indentation deformation is plastic, not elastic. In ceramics there is a more even balance of elastic and



plastic deformations<sup>11</sup> while in polymers and elastomers there may be little or no plastic deformation. In the case of an absence of plastic deformation, the “hardness” can still be computed as the mean contact stress, although obviously there is no residual impression to measure and the contact radius at maximum load must be inferred from a calibration function.

In elastic-plastic indentation testing, as in metals, ceramics and to some extent glassy polymers, it is desirable to separate the elastic and plastic deformation components to allow for calculations of the elastic modulus as well as the hardness. Key developments in this field were made by Doerner and Nix<sup>12</sup> prior to the landmark work of Oliver and Pharr<sup>1</sup>. The Oliver-Pharr procedure is most commonly employed for conical or pyramidal indentation, although it is occasionally used for spherical indentation. A second elastic-plastic deconvolution scheme for spherical indentation is that of Field and Swain<sup>13</sup>, which will be mentioned briefly. In this section, the mechanisms for measuring elastic modulus in elastic-plastic materials will be considered, along with procedures for identifying plastic deformation and for quantifying the plasticity in terms of hardness.

#### ***4.1. Elastic-Plastic Spherical Contact***

In spherical indentation, there is a change in the functional form of the load-displacement relationship from  $P \sim h^{3/2}$  to  $P \sim h$  when deformation shifts from elastic to plastic. This change is clearly evident in soft, single crystal aluminum; nanoindenter data from fused silica glass and aluminum have been plotted on a log scale along with lines indicating the two critical functional forms of the load-displacement relationship for spherical indentation. The aluminum data clearly demonstrates the transition to  $P \sim h$  behavior (Figure 5-4) while the glass data (the same response as in Fig. 5-3) retains the elastic functional form.

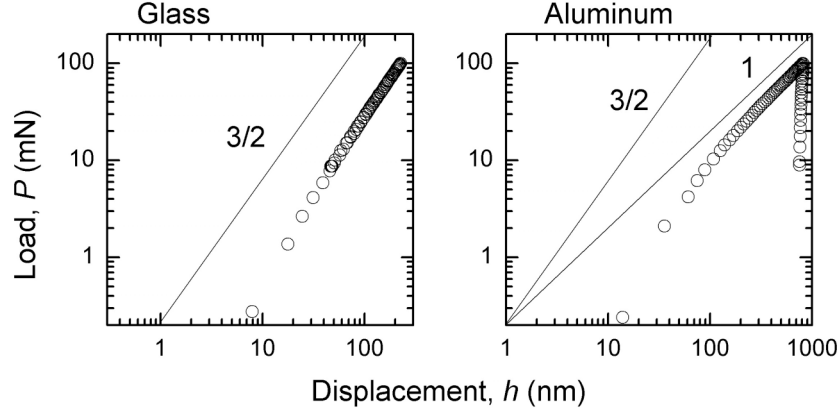


Figure 5-4. Elastic-plastic indentation responses for a sphere on fused silica glass and aluminum. The fused silica remains elastic while the aluminum demonstrates the onset of plastic deformation and a transition from  $P \sim h^{3/2}$  to  $P \sim h$  behavior at displacements above 100 nm displacement.

In spherical indentation of elastic-plastic materials, the separation of elastic and plastic deformation responses is performed utilizing a procedure that utilizes a modification of the Hertzian elastic expression (Eqn. 5-5) based on an assumption of elastic unloading<sup>13</sup>.

$$E_R = \frac{3}{4} \frac{P}{h_e^{3/2}} \left( \frac{1}{R} - \frac{1}{R'} \right)^{1/2} \quad (5-10)$$

where  $h_e$  is the elastic penetration depth and

$$\left( \frac{1}{R} - \frac{1}{R'} \right) \quad (5-11)$$

is the relative curvature between the indenter and the residual impression on the sample surface. The challenge lies in identifying the elastic depth  $h_e$  as a function of the total depth, and separating out this relative curvature term. In this regard a “partial unloading” protocol has been developed for using multiple loading and (partial) unloading cycles—a stepwise indentation protocol—to assist with identification of the plastic depth and allow for elastic modulus measurements. The interested reader is referred to Ref. 13 for further details; in many cases the

advantage of using a spherical indentation probe is the avoidance of the onset of plastic deformation. For this reason spherical probes are often used for elastic, viscoelastic and poroelastic analysis and less commonly for elastic-plastic problems.

#### 4.2. *E and H Deconvolution for Sharp Indentation*

Elastic-plastic indentation testing typically uses a sharp “geometrically similar” pyramidal (or, less commonly, conical) probe with a fixed cone angle (Fig. 5-1). For conical pyramidal indentation with very sharp probe tips (indenter radius  $R_i = 50\text{-}100\text{ nm}$ ), the large strains in the material below the point results in a near-immediate onset of plasticity and a dominantly plastic overall response. The functional form for elastic and plastic deformation are both  $P \sim h^2$  under conical or pyramidal loading, further complicating the distinction (Figure 5-5) and making it impossible to separate these deformation components by functional form in the same manner as for spherical indentation. As mentioned briefly above, the parameter generically called “hardness” ( $H$ ) is frequently used to characterize dominantly plastic materials<sup>10</sup>.

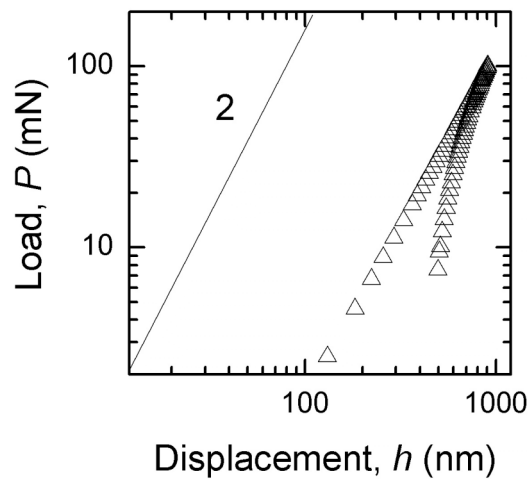


Figure 5-5. Elastic-plastic indentation responses for a Berkovich on glass demonstrating a consistent  $P \sim h^2$  response across the entire loading trace. The unloading trace has a different, and changing, functional form.

The overall scheme for separating elastic and plastic deformations in the Oliver-Pharr method is based on the assumption that the unloading response is purely elastic, such that the reduced modulus  $E_R$  (Eqn. 5-3) of the contact can be related to the unloading stiffness  $S$  (Fig. 5-6) via:

$$E_R = \frac{S\sqrt{\pi}}{2\sqrt{A_c}} \quad (5-12)$$

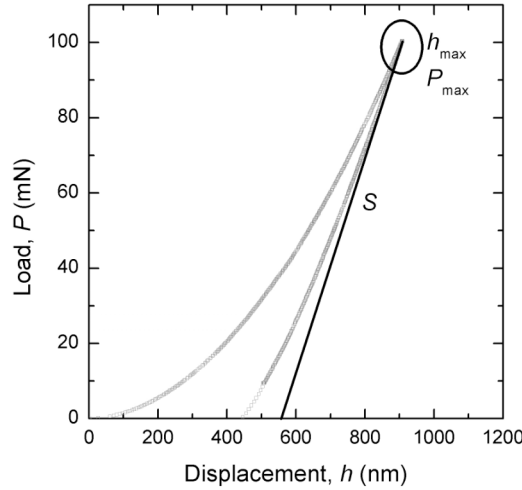


Figure 5-6. Elastic-plastic indentation responses for a Berkovich on fused silica glass, illustrating the three parameters taken directly from the load-displacement ( $P$ - $h$ ) response for Oliver-Pharr<sup>1</sup> analysis:  $h_{\max}$ ,  $P_{\max}$ ,  $S$ .

In Eqn. 5-12 the contact area ( $A_c$ ) appears, where the contact area is the projected area calculated from the contact displacement ( $h_c$ ) via a calibration function of the form  $A_c = A_c(h_c)$ . In Eqn. 5-9, it was assumed for both a four-sided pyramid and a three-sided pyramid that the indenter was infinitely sharp and the relationship between  $A_c$  and  $h_c$  did not change with indenter depth. However, in reality the relationship is flawed at small indenter depths, due to the so-called “tip imperfection” where a sharp pyramid cannot be physically made to be infinitely sharp, and is therefore more of a blunt sphere at some small contact depth  $h_c$ .

and the hardness is defined as  $H_c = P_{\max}/A_c(h_c)$ . In the classic Oliver and Pharr<sup>1</sup> analysis, the relationship between contact depth and contact area is often taken as a summed polynomial of the form

$$A_c(h_c) = C_0 h_c^2 + \sum_{k=1} C_k h_c^{1/2(k-1)} \quad (5-13)$$

in which the coefficients  $C_i$  are determined by calibration. Other functional forms are possible, such as the physically-meaningful<sup>14</sup>:

$$A_c(h_c) = (\pi \tan^2 \psi) h_c^2 + 4R\pi h_c + 4R^2 \pi \cot^2 \psi \quad (5-14)$$

from the harmonic average of two tip geometries and in which the only two parameters are the effective tip radius  $R$  and the included cone angle  $\psi$ . Of course, this expression is less useful at extremely small indentation depths since it gives  $A_c(h_c) \neq 0$  at  $h_c = 0$ , but it is very effective in estimating a tip effective radius. Any area function  $A_c(h_c)$  can be determined by solving the  $E_R$ - $S$  relationship (Eqn. 5-12) for  $A_c$  at each contact depth  $h_c$ :

$$h_c = h_{\max} - 0.75 \frac{P_{\max}}{S} \quad (5-15)$$

assuming the fixed value of  $E_R$  for a material with known (and constant with depth) elastic modulus (and thus reduced modulus). This calibration standard is typically the glass fused silica (a.k.a. fused quartz) with an elastic modulus  $E = 72$  GPa and Poisson's ratio  $\nu = 0.17$  such that, with diamond ( $E = 1.02$  TPa and  $\nu = 0.07$ ) the reduced modulus  $E_R = 69.6$  GPa.

In addition to the area function, there is an additional calibration-derived quantity, the machine (frame) compliance. The measured stiffness,  $S$ , is the series combination of the sample stiffness,  $S_s$ , and the frame compliance,  $S_f$ , as:

$$\frac{1}{S} = \frac{1}{S_s} + \frac{1}{S_f} \quad (5-16)$$

The contact area ( $A_c$ ) and the frame compliance ( $C_f = S_f^{-1}$ ) are related, and the calibration protocol used to obtain these values has been discussed at length in other sources<sup>1</sup> and even in the manuals for commercial nanoindentation instruments.

Once the full calibration (frame compliance and tip area function) is known, the analysis of elastic-plastic DSI data using the Oliver-Pharr protocol is straightforward. Three parameters are obtained directly from raw  $P$ - $h$  data, the peak load ( $P_{\max}$ ), the peak displacement ( $h_{\max}$ ) and the unloading stiffness ( $S = dP/dh$ ) as shown in Figure 5-6. The measured stiffness  $S$  is corrected by eqn. 5-16 to obtain the sample stiffness and the contact depth ( $h_c$ ) is computed from Eqn. 5-15. The corresponding contact area  $A_c(h_c)$  is calculated from the area calibration (Eqn 5-13 or 5-14) and used to calculate properties of reduced modulus (Eqn 5-12) and the contact hardness ( $H_c = P_{\max}/A_c$ ). Typically, in commercial indentation instruments the full procedure is carried out in the background, such that the output to the instrument operator is simply the properties ( $E_R$  and  $H_c$ ) as a function of depth ( $h_c$ ) assuming the frame compliance and area functions were programmed into the instrument.

## 5. Elastic Contact of Complex Materials and Systems

The elastic solutions presented in section 3 were for indentation of a homogeneous isotropic elastic half-space. Before moving on to examine more complicated material constitutive behavior, such as viscoelastic materials, we will first briefly mention elastic indentation in three cases that frequently arise in the context of biological tissues: anisotropic materials, inhomogeneous (composite) materials and layered systems (i.e. thin films on substrates). Unsupported membrane systems will be considered in chapter 10 of this volume, and will therefore be excluded from the current discussion.

### 5.1. Anisotropic Materials

Indentation of an anisotropic material has been considered in explicit analytical formulations<sup>15,16</sup> and experimentally for bone<sup>17</sup>. The premise is that the anisotropic indentation modulus,  $M$ , is defined where  $M$  is specific to the orientation of the anisotropic material being indented, with the limiting case that  $M = E/(1 - \nu^2)$  for an isotropic material. Analogous to the relationship between reduced (or plane strain) modulus in eqn 5-12,

$$M = \frac{S\sqrt{\pi}}{2\sqrt{A_c}} \quad (5-17)$$

The indentation modulus  $M$  is defined in the context of the ratio of radii of the projected contact,  $a_1/a_2$  (Fig. 5-7). The solution for the indentation modulus is a complicated integral expressions over components  $B_{ij}$  derived from the stiffness matrix ( $C_{ij}$ ):

$$M = \frac{4\pi}{\int_0^{2\pi} \frac{a_{3i} B_{ij}^{-1}(\gamma) a_{3j}}{[(a_1/a_2) \cos^2 \gamma + (a_2/a_1) \sin^2 \gamma]} d\gamma} \quad (5-18)$$

where  $a_{3i}$  and  $a_{3j}$  are the direction cosines of the angles between the indentation direction and the elastic stiffness matrix. The expression must be solved numerically and therefore is not easily implemented in routine data analysis. Commonly reported are simply the effective indentation modulus for different orientations, in which the results are not converted back to components of the stiffness tensor ( $C_{ij}$ ). Overall, the indentation modulus varies less with orientation than does the effective elastic modulus, where the maximum indentation modulus is less than the maximum apparent modulus in tension and the minimum indentation modulus is greater than the apparent modulus in tension<sup>17</sup>.

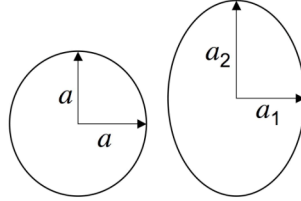


Figure 5-7. Projected contact area for an isotropic and anisotropic material following spherical or pyramidal indentation. For the isotropic case, the contact radii in perpendicular directions are equal ( $a = a$ ) whereas for the anisotropic case  $a_1 \neq a_2$ .

## 5.2. Inhomogeneous Materials

Two features differentiate the indentation responses of composite materials (*i.e.* materials with two or more distinct phases) compared with homogeneous materials. First, a length-scale is introduced, in the form

of the size of the features of the multiphase material (Figure 5-8 where the feature size is the particle radius  $r$ ). Second, there is a critical dependence on indenter tip placement in terms of the observed indentation response, especially at small indentation depths where the indentation contact radius  $a$  or contact depth  $h_c$  is comparable in scale to the composite feature size  $r$ . Several recent studies have explicitly examined indentation of materials with substantial heterogeneity<sup>18-20</sup>. The general approach involves the sampling of a large number of individual indentation responses across the material surface and using the obtained range of responses to bound the inferred microstructure in terms of phase length-scale<sup>18</sup> and mechanical properties<sup>19</sup>. Substantially more effort is required to develop a robust method for the mechanical characterization of composite materials by indentation without the need for finite element analysis<sup>20</sup>.

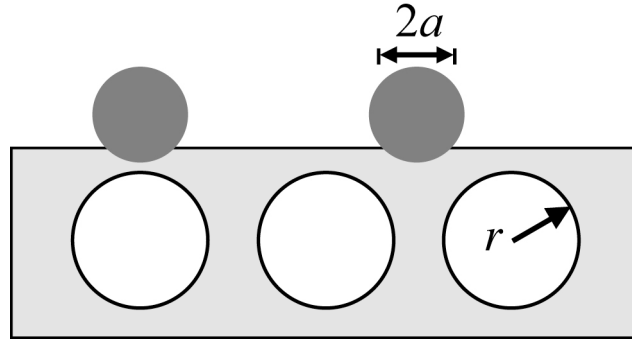


Figure 5-8. Schematic illustration of indentation of a composite material, in which the observed response depends on the placement of the indenter relative to microstructural features and the relative indentation and microstructural length-scales ( $a$  vs  $r$ ).

### 5.3. Layered Systems

The analyses presented thus far have been oriented towards bulk materials. However, in the majority of soft tissue indentation tests, the soft tissue layer of interest (*e.g.* cartilage) is supported by a much stiffer substrate (frequently bone). Just as in the case of composite materials, the indentation of a layered structure introduces a length-scale into the indentation problem, where the indentation contact depth or contact radius ( $h_c$  or  $a$ , respectively) are considered relative to the layer thickness



( $t_f$ ). The most commonly employed analysis for soft tissue indentation testing relies on the finite thickness of the tissue layer, considering the underlying bone as a rigid substrate<sup>21</sup>. The elastic expression employed for analysis is thus a modification of the bulk flat-punch elastic solution (Eqn. 5-7) and is written:

$$P = \kappa 2R \frac{E}{(1 - \nu^2)} h \quad (5-19)$$

where  $\kappa = \kappa(\nu, R / t_f)$ . In this instance, the contact dimension is fixed and  $R = a$ . The original work<sup>21</sup> required a look-up table to determine values of  $\kappa$  based on the numerical solution, but of course in the intervening years the analysis for the film-substrate problem has become near routine, at least in the instance in which the modulus mismatch between the film and substrate ( $E_f/E_s$ ) is not more than an order of magnitude. The problem of larger modulus mismatch has also been examined within a framework of analytical elasticity<sup>22</sup>. In practice, it is common to use relatively simple empirical functions to extrapolate apparent elastic modulus-depth data to estimate the modulus of a thin layer<sup>23</sup> or to keep the indentation depth well below 10% of the total layer thickness<sup>1</sup>.

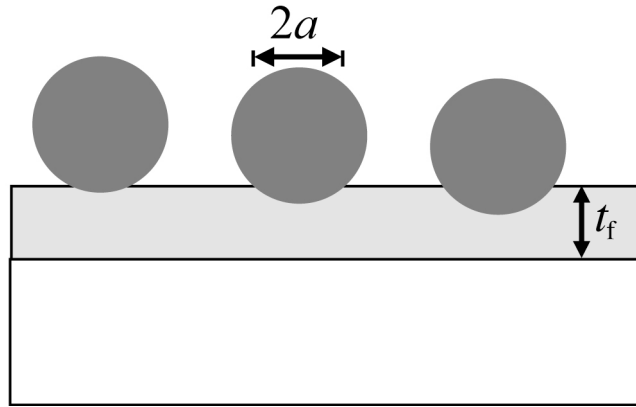


Figure 5-9. Schematic illustration of indentation of a layered structure, in which the observed response depends on the ratio of the indentation length-scale (as given by either the indentation depth  $h$  or contact radius  $a$ ) relative to the layer thickness ( $t_f$ ).

## **6. Time-Dependent Contact**

A complication arises in the application of nanoindentation techniques for examination of biological materials, in that substantial time-dependent deformation can occur during the experimental time-frame. As such, the assumption of elastic unloading in the Oliver-Pharr procedure is violated, and different analyses must be employed. Time-dependent deformation appears most readily in nanoindentation data as increasing creep displacement at fixed load; in some cases, further forward displacement can be seen during unloading, a feature that has been termed a “nose” in the curve<sup>24</sup>. When experiments are conducted in displacement control instead of load control, the time-dependence is seen as load relaxation at fixed depth, and no “nose” is present in the data. Related to the existence of time-dependent deformation observed at fixed load or displacement, there are clear differences observed in the load-displacement response of time-dependent materials when probed at different load- or displacement- rates.

In this section, two mechanisms of time-dependent deformation will be explored, viscoelasticity and poroelasticity. Empirical viscoelastic approaches will be presented first, addressing both linear and nonlinear viscoelasticity. Mechanism-driven poroelastic approaches will then be considered, in which the time-dependent deformation is explicitly associated with fluid flow through a porous elastic network.

### **6.1. Viscoelastic Contact**

There are two limits to the elastic modulus in all materials, the adiabatic modulus and the isothermal modulus. In relatively time-independent materials, the two limits are comparable and the difference is not easily noted in routine mechanical testing experiments. In time-dependent materials, the two limits can be widely divergent and the region of transition between the limits can be complicated. As it is experimentally impossible to measure mechanical properties either infinitely quickly or infinitely slowly, the apparent elastic modulus of a viscoelastic material is changing with time over reasonable experimental time-frames. A full physical and mechanistic model for viscoelastic

behavior remains elusive; for engineering practice, it is common to fit the elastic modulus-time responses to empirical functions based on simple mathematical constructs such as an exponential decay or a power-law decay in time.

### 6.1.1. Linearly viscoelastic materials

The time-dependent mechanical behavior of polymeric and many biological materials is often represented with a mechanical model formed of spring elements that are linear elastic (Hookean):

$$\sigma = G\varepsilon \quad (5-20)$$

and linearly viscous (Newtonian) “dashpots”:

$$\sigma = \eta \frac{d\varepsilon}{dt} \quad (5-21)$$

Combinations of these simple relationships are made in arranging springs and dashpots in series and parallel configurations (Fig. 5-10) and then solving for the stress-strain-time ( $\sigma$ - $\varepsilon$ - $t$ ) relationship, a differential equation in time.

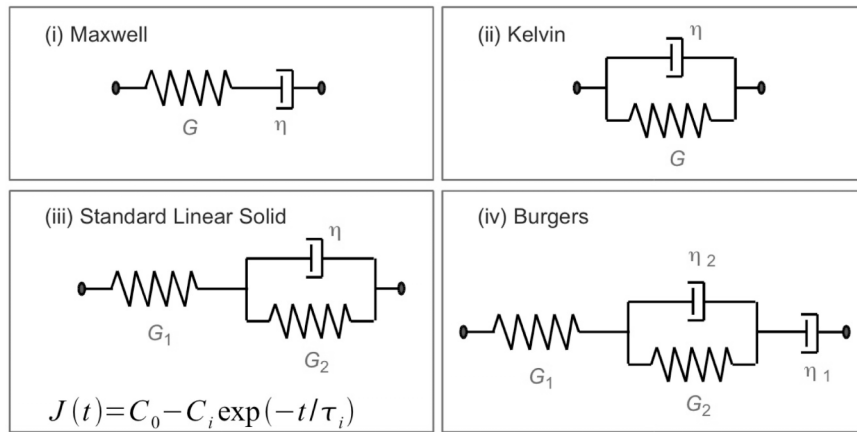


Figure 5-10. Examples of linear viscoelastic models formed from combinations of springs and dashpots with their independent constitutive responses as in Eqns. 5-20 and 5-21.

The order of the differential equation depends on the number of individual dashpots in the full system: the standard linear solid model has

a first order differential equation constitutive response while the Burgers model is second order. From this constitutive relationship the homogeneous (single-axis, uniform loading) creep and relaxation functions can be obtained by solving the stress-strain-time ( $\sigma$ - $\varepsilon$ - $t$ ) relationship for a condition of step stress

$$\sigma(t) = \sigma_0 H(t) \quad (5-22)$$

or step strain

$$\varepsilon(t) = \varepsilon_0 H(t) \quad (5-23)$$

where the  $H(t)$  is the Heaviside step function. From this time-dependent response to a step input, the relaxation function  $G(t)$  and creep function  $J(t)$  are defined as

$$\frac{\sigma(t)}{\varepsilon_0} = G(t) \quad (5-24)$$

$$\frac{\varepsilon(t)}{\sigma_0} = J(t) \quad (5-25)$$

These functions typically have a quite simple summed exponential functional form for linearly viscoelastic solids (*i.e.* those defined by a combination of linear springs and dashpots) even when many elements are present, such that they can be generalized as

$$G(t) = C_0 + \sum C_i \exp(-t / \tau_i) \quad (5-26)$$

$$J(t) = C_0 - \sum C_i \exp(-t / \tau_i) \quad (5-27)$$

The creep and relaxation functions are related in the time domain at their endpoints only:

$$G(0) = J(\infty)^{-1}, \quad G(\infty) = J(0)^{-1}, \quad G(t) \neq J(t) \quad (5-28)$$

In many cases, it is of limited value to try and relate the coefficients  $C_k$  back to individual spring and dashpot terms in a 1-D mechanical model representation, with the exception of a free spring defining either an instantaneous or infinite time modulus value [*i.e.*  $G(0)$  or  $G(\infty)$ ].

### 6.1.2. Linear viscoelastic indentation correspondence

The development of viscoelastic functions here has been for relationships between single scalar stress and strain components. In adapting this viscoelastic approach for three-dimensional stress and strain analysis, these basic functional forms are assumed to hold between individual tensor components of the overall stress and strain tensors. In practice, indentation problems are most commonly written in the single scalar form relating axial load to axial displacement, and in this context the conversion from viscoelastic stress-strain space to axial load-displacement space is trivial.

Approaches to the analytical viscoelastic indentation problem utilize the correspondence between elastic and viscoelastic elasticity problems<sup>25,26</sup>; the only difference between an elastic and a viscoelastic problem is in the choice of a time-dependent constitutive law for the material<sup>26</sup>. Elastic-viscoelastic correspondence analysis was examined within the context of the Hertzian contact problem by Lee and Radok<sup>27</sup> and is summarized in Johnson's text<sup>4</sup>. For analysis of indentation loading conditions in which the contact area is non-decreasing, the problem is fairly straightforward; for decreasing contact areas an adapted analysis<sup>28</sup> is required. Since the two most common time-dependent experiments (creep or relaxation at fixed load or displacement, or loading at various load- or displacement-rates) are for non-decreasing contact areas, the straight-forward analysis of Lee and Radok<sup>27</sup> is the sole analysis considered here in the context of elastic-viscoelastic correspondence.

The elastic solutions for indentation—written in terms of an axial load and axial displacement—are rewritten as viscoelastic expressions by replacing the elastic constants by viscoelastic operators, and integrating over the applied load- or displacement-perturbation. For the viscoelastic indentation analysis, an elastic indentation solution (Eqns. 5-5,7,8) is rewritten in terms of the shear modulus, where  $G = E/[2(1+\nu)]$  for the general case (requiring fixed Poisson's ratio) and  $G = E/3$  for the incompressible case (and the plane strain modulus thus equates to  $4G$ ). From this point we will emphasize the incompressible case; data can

always be back-corrected in the instance where the Poisson's ratio is known (and known to be less than 0.5)<sup>29</sup>.

In cases where step-loading can be assumed, there is a straightforward replacement of  $P/2G$  with the product of the creep load,  $P_0$ , and the creep function,  $J(t)$ :

$$h = \frac{1}{4R} \left[ \frac{P}{2G} \right] \rightarrow h(t) = \frac{1}{4R} P_0 J(t) \quad (5-29)$$

$$h^{3/2} = \frac{3}{8\sqrt{R}} \left[ \frac{P}{2G} \right] \rightarrow h^{3/2}(t) = \frac{3}{8\sqrt{R}} P_0 J(t) \quad (5-30)$$

$$h^2 = \frac{\gamma^2}{\pi \tan \psi} \left[ \frac{P}{2G} \right] \rightarrow h^2(t) = \frac{\gamma^2}{\pi \tan \psi} P_0 J(t) \quad (5-31)$$

For “real” loading conditions, there is a finite ramping time or ramping rate up to the peak load. In this case, a hereditary integral formulation is used, where integration takes place over the creep function and the applied loading history  $P(t)$ . For the general indentation, indentation and load-control, this amounts to replacing  $P/2G$  with an integral over the creep compliance function and applied loading conditions:

$$h = \frac{1}{4R} \left[ \frac{P}{2G} \right] \rightarrow h(t) = \frac{1}{4R} \int_0^t J(t-u) \frac{dP(u)}{du} du \quad (5-32)$$

$$h^{3/2} = \frac{3}{8\sqrt{R}} \left[ \frac{P}{2G} \right] \rightarrow h(t) = \left[ \frac{3}{8\sqrt{R}} \int_0^t J(t-u) \frac{dP(u)}{du} du \right]^{2/3} \quad (5-33)$$

$$h^2 = \frac{\gamma^2}{\pi \tan \psi} \left[ \frac{P}{2G} \right] \rightarrow h(t) = \left[ \frac{\gamma^2}{\pi \tan \psi} \int_0^t J(t-u) \frac{dP(u)}{du} du \right]^{1/2} \quad (5-34)$$

As can be seen from the forms of equations 5-32 to 5-34 is that the integral term  $\int_0^t J(t-u) \frac{dP(u)}{du} du$  is identical, and as such a single set of solutions for commonly used experiments, such as ramping at constant loading rate, or a creep test following a ramp, can be used in each geometry. For a ramp test where  $P(t) = kt$  the integral is simply over the creep function  $k \int_0^t J(t-u) du$  and the exponential representation of the

creep function (Eqn 5-27) makes the integration trivial. Solutions for multiple-stage indentation tests, such as a stair-step creep test at several (increasing) peak loads, involves a substantial book-keeping effort but relatively simple calculus<sup>30</sup>: solutions maintain the exponential functional form of the creep function and are thus relatively easy to implement experimentally. For example<sup>30,31</sup> for spherical indentation creep following a ramp to peak load  $P_{\max}$  in time  $t_R$  (such that the loading rate is constant and equal to  $k = P_{\max}/t_R$ ) the solution for displacement-time can be written in the compact form:

$$h^{3/2}(t) = \frac{3P_{\max}}{8\sqrt{R}} \left[ C_0 - \sum C_i \exp(-t/\tau_i) \text{RCF}_i \right] \quad (5-35)$$

$$\text{RCF}_i = \frac{\tau_i}{t_R} \left[ \exp(t_R/\tau_i) - 1 \right] \quad (5-36)$$

where  $\text{RCF}_i$  is a dimensionless “ramp correction factor”<sup>30</sup>; comparison of eqns. 5-35 and 5-30 illustrates that this factor fully accounts for a finite ramping time instead of an assumption of step loading.

Recall that the restriction on this simple mathematical approach<sup>27</sup> is that the contact area is non-decreasing such that unloading is not a focus. A different approach to the same problem<sup>28</sup> a few years later yielded a complementary solution that does not carry the restriction and allows for full unloading analysis in a linearly viscoelastic material. A further discussion on these two approaches in the context of indentation viscoelasticity is available<sup>32</sup>.

For displacement controlled testing, under a step displacement  $h(t) = h_0$   $H(t)$  the load-time relationship is again trivial by the substitutions paralleling those used in Eqns 5-29 to 5-31:

$$P = 4Rh_0G(t) \quad (5-37)$$

$$P(t) = \frac{8\sqrt{R}}{3} h_0^{3/2} G(t) \quad (5-38)$$

$$P(t) = \frac{\pi \tan \psi}{\gamma^2} h_0^2 G(t) \quad (5-39)$$

However, the hereditary integral approach is slightly more complicated. The form of the integral depends on the linearity or nonlinearity of the

load-displacement relationship—integration is conducted over  $2Gh^m$  where  $m$  is the power law exponent for the indentation load-displacement relationship:

$$P = 4R2Gh \rightarrow P(t) = 4R \int_0^t G(t-u) \frac{dh(u)}{du} du \quad (5-40)$$

$$P = \frac{8\sqrt{R}}{3} 2Gh^{3/2} \rightarrow P(t) = \frac{8\sqrt{R}}{3} \int_0^t G(t-u) \frac{dh^{3/2}(u)}{du} du \quad (5-41)$$

$$P = \frac{\pi \tan \psi}{\gamma^2} 2Gh^2 \rightarrow P(t) = \frac{\pi \tan \psi}{\gamma^2} \int_0^t G(t-u) \frac{dh^2(u)}{du} du \quad (5-42)$$

This nonlinearity can result in integral expressions with no closed form solution, particularly in a spherical indentation configuration<sup>33</sup>.

The expressions here considered the case of bulk material indentation in that the elastic solutions used were applicable to an elastic half-space. However, it is equally possible to use this correspondence approach in the context of other elastic solutions, such as a layered system. Such an approach has been extremely common in flat-punch indentation for a soft layer on a stiff underlayer, such as articular cartilage on bone<sup>21</sup> or a polymer thin film on a silicon substrate<sup>34</sup>.

### 6.1.3. Viscous-Elastic-Plastic Materials

In sharp indentation problems, especially when the materials considered are glassy polymers, plastic deformation may be present along with viscoelastic deformation. Two general approaches have been used to address this plastic deformation in the viscoelastic data analysis. The first mechanism is to remove the plastic deformation component from consideration using a load-unload-reload protocol<sup>35</sup>, in which the reloading segment is assumed to be purely viscoelastic. Alternately, the plastic deformation can be modeled explicitly and thus included as an additional parameter in the analysis. A viscous-elastic-plastic series model with independent elements for each deformation mode has been developed<sup>36</sup>. In its simplest incarnation, the model incorporates three independent deformation components such that the total displacement during loading is the sum of the component displacements:



$$h = h_v + h_e + h_p \quad (5-43)$$

There are three defining material properties, one associated with each deformation component (a plane strain elastic modulus  $E'$ , a resistance to plastic deformation  $H$ , and a viscous time constant  $\tau_Q$ ). For constant loading-rate indentation testing where  $P(t) = kt$ ,  $k = \text{constant}$ ,

$$h_{\text{load}}(t) = \left[ \frac{1}{(\alpha_2 E')^{1/2}} + \frac{1}{(\alpha_1 H)^{1/2}} + \frac{2t}{3\tau_Q (\alpha_2 E')^{1/2}} \right] (kt)^{1/2} \quad (5-44)$$

where the  $\alpha_i$  values are dimensionless constants related to the indenter included angle<sup>36</sup>. For a load reversal at  $t = t_R$  (i.e. the second phase of a triangle-wave test, Figure 5-2b), the load-time response is:

$$\begin{aligned} h_{\text{unload}} = & \left[ \frac{1}{(\alpha_2 E')^{1/2}} + \frac{1}{(\alpha_1 H)^{1/2}} + \frac{2t_R}{3\tau_Q (\alpha_2 E')^{1/2}} \right] (kt_R)^{1/2} \\ & + \frac{1}{(\alpha_2 E')^{1/2}} \left[ (2kt_R - kt)^{1/2} - (kt_R)^{1/2} \right] \\ & - \frac{2}{3k\tau_Q (\alpha_2 E')^{1/2}} \left[ (2kt_R - kt)^{3/2} - (kt_R)^{3/2} \right] \end{aligned} \quad (5-45)$$

This approach has also been expanded to incorporate the effects of a polymer film on a stiff and time-independent elastic substrate<sup>37</sup>.

### 6.1.3. Dynamic Contact Measurements

In the case of dynamic sinusoidal loading for frequency-based measurements, the input is an oscillation at force amplitude  $P_0$ , where the value  $P_0$  is a small perturbation on the primary peak force  $P_{\text{max}}$  such that  $P_0 \ll P_{\text{max}}$  and  $P(t) = P_{\text{max}} + P_0 \sin(\omega t)$  for frequency  $\omega$ . The response is a displacement of amplitude  $h_0$  and a phase shift  $\phi$  such that the response to the load perturbation has an  $h(t) = h_0 \sin(\omega t - \phi)$  dependence. The real, or storage ( $E_s$ ) and imaginary, or loss ( $E_L$ ) parts of the elastic modulus are then calculated where the complex modulus is  $E^* = E_s + i E_L$  and

$$\frac{E_s}{(1 - \nu^2)} = \frac{S\sqrt{\pi}}{2\sqrt{A_c}} \quad (5-46)$$

$$\frac{E_L}{(1-\nu^2)} = \frac{\omega D \sqrt{\pi}}{2\sqrt{A_c}} \quad (5-47)$$

analogous to Eqn. 5-12 and where  $D$  is a damping coefficient. The real and imaginary moduli can be calculated directly from

$$E_s = (1-\nu^2) \frac{\sqrt{\pi}}{2\sqrt{A_c}} \left| \frac{P_0}{h_0} \right| \cos \phi \quad (5-48)$$

$$E_L = (1-\nu^2) \frac{\sqrt{\pi}}{2\sqrt{A_c}} \left| \frac{P_0}{h_0} \right| \sin \phi \quad (5-49)$$

The derivations of these expressions and caveats concerning their use can be found in other sources<sup>38-40</sup>. In practice, the typical experiment would include a number of different measurements for different frequencies (“frequency sweep”) and the evaluation of the real and imaginary parts of the complex modulus as a function of frequency and potentially also as a function of static ( $P_{\max}$ ) and dynamic ( $P_0$ ) load levels.

## 6.2. Poroelastic Contact

Poroelasticity concerns the flow of fluid through a saturated porous elastic solid<sup>41</sup>. Although the components (fluid, solid) themselves are taken to be time-independent, the flow problem creates time-dependence. The basic elastic problem is augmented in poroelasticity with two additional scalar variables, the pore pressure,  $p$ , and an increment of fluid content,  $\zeta$ , the change in fluid volume relative to a control volume. The poroelastic framework considered here is for an isotropic elastic porous material with elastic material properties shear modulus,  $G$ , and Poisson’s ratio,  $\nu$ . There are two other parameters to characterize the fluid and the fluid-solid interactions,  $\alpha$  and  $B$ , which are bounded between zero and unity. With the additional variables ( $p$ ,  $\zeta$ ) and material constants ( $\alpha$ ,  $B$ ), the stress-strain ( $\sigma_{ij} - \varepsilon_{ij}$ ) relationship for elasticity is modified by the addition of a term including the pore pressure ( $\alpha p \delta_{ij}$ ) to become:

$$\sigma_{ij} + \alpha p \delta_{ij} = 2G\varepsilon_{ij} + \left( \frac{2G\nu}{1-2\nu} \right) \varepsilon_{kk} \delta_{ij} \quad (5-50)$$

where  $\delta_{ij}$  is the Kronecker delta.<sup>26</sup> A single additional scalar expression is added to the six elastic equations to total seven constitutive equations:

$$2G\zeta = \alpha \left( \frac{1-2\nu}{1+\nu} \right) \left( \sigma_{kk} + \frac{3p}{B} \right) \quad (5-51)$$

The four parameters ( $G$ ,  $\nu$ ,  $\alpha$  and  $B$ ) make a complete set of material properties for a poroelastic solid; other sets of four parameters are possible and it is particularly useful to use a parameter set that includes  $\nu_u$ , the undrained Poisson's ratio. Finally, the permeability ( $\kappa$ ) is the parameter characterizing flow through the porous elastic skeleton in Darcy's law relating the flux ( $q_i$ ) to the pressure gradient ( $p_{,i}$ ) via the hydraulic permeability  $\kappa$ :

$$q_i = -\kappa p_{,i} \quad (5-52)$$

The equations of poroelasticity are coupled: a change in applied stress leads to a change in fluid pressure or mass, and a change in fluid pressure or mass leads to a change in the volume of the solid. Because of this coupling, the poroelastic problem can be solved analytically in only a few cases, such as homogeneous uniaxial creep. Numerical solutions<sup>42</sup> as well as computational approaches<sup>43</sup> have been particularly useful in combining the poroelastic equations with the indentation problem. Spherical indentation has been considered for characterizing hydrated bone<sup>6</sup> and acrylamide gels<sup>44</sup>, in both cases resulting in estimated hydraulic permeability values consistent with values measured using traditional (*i.e.* non-indentation) methods. The application of poroelastic material models to the routine analysis of indentation data is an area of active current research.

## 7. Conclusions and Outlook

This chapter has focused on the analysis of indentation data, with an emphasis on material behavior that deviates from the elastic-plastic responses typical of engineering ceramics and metals. In cases such as linear viscoelasticity, analysis of nanoindentation data has become routine, while new approaches are just emerging for poroelasticity. In general, when handling nanoindentation data for biological materials, it

is critical to identify the modes of deformation active during the indentation test, and to analyze the data appropriately for those deformation modes.

## References

1. Oliver WC and Pharr GM, *J. Mater. Res.* 7, 1564 (1992).
2. Oyen ML and Cook RF, *J. Mech. Behavior Biomed. Mater. In press* (2008). DOI: 10.1016/j.jmbbm.2008.10.002.
3. Davis RO and Selvadurai APS, *Elasticity and Geomechanics*. (Cambridge UK: Cambridge University Press, 1985)
4. Johnson KL, *Contact Mechanics*. (Cambridge UK: Cambridge University Press, 1996).
5. Bembey AK, Bushby AJ, Boyde A, Ferguson VL, Oyen ML, *J. Mater. Res.* 21, 1962 (2006).
6. Oyen ML, *Poroelastic Nanoindentation Responses of Hydrated Bone*. *J. Mater. Res.* 23, 1307 (2008).
7. Lucas BN, W.C. Oliver, G.M. Pharr, and L-L. Loubet, *Mater. Res. Soc. Symp. Proc.* 436, 233 (1997).
8. Hertz, H. *Miscellaneous Papers*, Translated by Jones, D.E. and Schott, G.A., (London UK, Macmillan and Co. Ltd., 1896).
9. Sneddon IN, *Int. J. Engng. Sci.* 3, 47 (1965).
10. Tabor D, *The Hardness of Metals* (London UK: Oxford University Press at the Clarendon Press, 1951).
11. Oyen M., *J. Biomech.*, 39, 2699 (2006).
12. Doerner MF and Nix WD, *J. Mater. Res.* 1, 601 (1986).
13. Field JS and Swain MV, *J. Mater. Res.* 8, 297 (1993).
14. Thurn J and Cook RF, *J. Mater. Res.* 17, 1143 (2002).
15. Vlassak JJ, Ciavarella M, Barber JR, Wang X. *J. Mech. Phys. Solids* 51, 1701 (2003).
16. Swadener JG and Pharr GM, *Phil. Mag.* 81, 447 (2001).
17. Swadener JG, Rho J-Y, and Pharr GM, *J. Biomed. Mater. Res.* 57, 108 (2001).
18. Oyen ML and Ko CC, *J. Mater. Res.* 23, 760 (2008).
19. Constantinides G, Ravi Chandran KS, Ulm F-J, Van Vliet KJ, *Mater. Sci. Eng. A* 430, 189 (2006).
20. Durst K, Goeken M, Vehoff H, *J. Mater. Res.* 19, 85 (2004).
21. W. Hayes, L. Keer, G. Herrmann, and L. Mockros, *J. Biomech.* 5, 541 (1972).
22. Rar 2002 Rar A., H. Song, and G.M. Pharr., *Mater. Res. Soc. Symp. Proc.* 695, 431 (2002).
23. Mencik J, Munz D, Quandt E, Weppelmann ER, Swain MV, *J. Mater. Res.* 12, 2475, 1997.

24. Briscoe BJ, Fiori L, Pelillo E, J. Phys. D: Appl. Phys. 31, 2395 (1998).
25. Findley WN, Lai J, and Onaran K, Creep and Relaxation of Nonlinear Viscoelastic Materials, (Dover, New York, 1989).
26. Mase GT and Mase GE, Continuum Mechanics for Engineers, 2nd Ed. (CRC, Boca Raton, FL, 1999).
27. Lee EH and Radok JRM, J. Appl. Mech. 27, 438 (1960).
28. Ting TCT: J. Appl. Mech. 88, 845 (1966).
29. Oyen ML, Phil. Mag. 86, 5625 (2006).
30. Oyen ML, J. Mater. Res. 20, 2094 (2005).
31. Oyen ML, Acta Mater. 55, 3633 (2007).
32. Tweedie C and Van Vliet KJ, J. Mater. Res. 21, 1576 (2006).
33. Mattice JM, Lau AG, Oyen ML, Kent RW, J. Mater. Res. 21, 2003 (2006).
34. Zhang CY, Zhang YW, Zeng KY, J. Mater. Res. 19, 3053 (2004).
35. Zhang CY, Zhang YW, Zeng KY, Shen L, 2005, J. Mater. Res. 20, 1597 (2005).
36. Oyen ML and Cook RF, J. Mater. Res. 18, 139 (2003).
37. Oyen ML, Cook RF, Moody NR, and Emerson JA. J. Mater. Res. 19, 2487 (2004).
38. Huang G, Wang B, Lu H, Mech. Time-Dep. Mater. 8, 345 (2004).
39. Cheng Y-T, Ni W, Cheng C-M. Phys. Rev. Lett. 97, 075506 (2006).
40. Herbert EG, Oliver WC, Pharr GM, J. Phys. D: Appl. Phys 41, 074021 (2008).
41. Wang HF, Theory of Linear Poroelasticity with Applications to Geomechanics and Hydrogeology. (New Jersey: Princeton University Press. 2000)
42. Agbezuge LK and Deresiewicz H, Israel J. of Tech. 12, 322 (1974).
43. Selvadurai APS, Int. J. Solids Structures 41, 2043 (2004).
44. Galli M, Comley KSC, Shean TAV, Oyen ML. J. Mater. Res. *in press* (2008).